Chemical Engineering Journal 527 (2026) 171811

Contents lists available at ScienceDirect

Chemical Engineering Journal

journal homepage: www.elsevier.com/locate/cej

Engineered conversion of TiN from 2D Ti_2C MXene: A tailored synthetic strategy for high-performance microsupercapacitor applications

Hafis Hakkeem [a,1], Shridhar Hegde [a,1], Erdenebayar Baasanjav [a], Johnbosco Yesuraj [a], Jae-Kwang Kim [b], Jung Sang Cho [c], Chandra Sekhar Rout [a,d,*], Sang Mun Jeong [a,e,*]

[a] Department of Chemical Engineering, Chungbuk National University, 1 Chungdae-ro, Seowon-Gu, Cheongju, Chungbuk, 28644, Republic of Korea
[b] Department of Energy Convergence Engineering, Cheongju University, Cheongju, 28503, Republic of Korea
[c] Department of Engineering Chemistry, Chungbuk National University, Cheongju, 361-763, Republic of Korea
[d] Centre for Nano and Material Sciences, Jain University, Jain Global Campus, Jakkasandra, Ramanagaram, Bangalore, 562112, India
[e] Advanced Energy Research Institute, Chungbuk National University, 1 Chungdae-ro, Seowon-Gu, Cheongju, Chungbuk, 28644, Republic of Korea

A B S T R A C T

Transition metal nitrides are of recent interest for energy storage applications due to its conductivity, chemical stability and pseudocapacitance. However, the low surface area and oxidation susceptibility limits its extensive use. Herein, we propose a new synthesis route for Titanium nitride (TiN) from MXene (Ti_2C), where TiN holds on to the morphological advantages of MXene. The accordion structured TiN, modified with carbon agglomerations promises high surface area for better electrode-electrolyte interaction. MXene is annealed with a mixture of urea, polyethylene glycol (PEG) and boric acid to obtain TiN. A detailed XRD and XPS study revealed that urea serves as the nitrogen source, PEG facilitates carbon agglomerations and boric acid acts as an oxidation inhibitor during synthesis. A promising specific capacitance of 23 mF cm^{-2} was attained in a three-electrode configuration, retaining 84 % of its initial value after 10,000 charge/discharge cycles. Furthermore, a symmetric microsupercapacitor device was fabricated, which shows 10 mF cm^{-2} specific capacitance with energy density of 632 μWh cm^{-3} at a power density of 19 mW cm^{-3}. The device exhibits dominant EDLC behavior with robust electrochemical stability, as evidenced by 94 % capacitance retention and 95 % coulombic efficiency after 10,000 charge–discharge cycles.

1. Introduction

Transition metal nitrides have been a recent interest for energy storage device owing to their low cost, conductivity, chemical stability and pseudocapacitance. Partially filled d orbitals of the transition metals enables surface redox reactions, while the d band crossing Fermi level imparts semi-metallic conductivity. Moreover, the presence of nitrogen enhances its corrosion resistance, rendering the material chemically stable and less prone to degradation. These factors make TMNs a favorable candidate for electrochemical energy storage devices. Nitrides of titanium, vanadium and molybdenum are being widely explored in recent times, not only for its energy storage applications but for other fields like catalysis, photonics, sensors, protective coatings etc. [1,2,3,4]. Among TMNs, Titanium nitride is one of the most favored material for energy storage devices when stability, conductive scaffold and reproducibility are prioritized. TiN combined with MXene is used for its adsorption capacity and catalytic effect in Li—S batteries by Luo et al. [5]. Pyramidal structured TiN film, reactively sputtered, exhibited excellent pseudocapacitive behavior, with good cyclic stability and conductivity [6]. Several more works on TiN and TiN based composites as energy storage material have been reported before [7].

Chemical vapor deposition (CVD), atomic layer deposition (ALD) and magnetron sputtering are some of the prominent methods to synthesize TiN films [8]. Mouchani et al. prepared TiN/TiON nanotubes by plasma enhanced CVD method for supercapacitor applications, with 85 % capacitance retention after 6000 cycles [9]. Hao et al. synthesized titanium nitride thin films grown on Si substrate by DC magnetron sputtering method. The SiNWs/TiN electrode showed high specific capacitance of 113.55 F g^{-1} and a capacitance decay of 12.4 % after 2000 cycles [10]. These methods often involve hazardous and expensive precursors like $TiCl_4$, TDMAT, Ti target etc. Although widely employed, the high capital cost of equipment and inability to produce bulk quantities makes these methods less attractive for scalable synthesis. Electrochemical deposition has also been employed as a synthesis route for TiN in various applications, including supercapacitors and the hydrogen evolution reaction (HER) [11]. In some cases, anodization is used to

* Corresponding authors at: Department of Chemical Engineering, Chungbuk National University, 1 Chungdae-ro, Seowon-Gu, Cheongju, Chungbuk, 28644, Republic of Korea.
E-mail addresses: r.chandrasekhar@jainuniversity.ac.in (C.S. Rout), r.chandrasekhar@jainuniversity.ac.in (S.M. Jeong).
[1] HH and SH contributed equally.

https://doi.org/10.1016/j.cej.2025.171811
Received 30 July 2025; Received in revised form 17 November 2025; Accepted 10 December 2025
Available online 11 December 2025

generate oxide precursors of titanium and molybdenum, which are subsequently converted into their respective nitrides [12]. Rahman et al. used electrochemical deposition technique to synthesis TiN supercapacitor electrodes which delivers 53.66 mF s^{-2} specific capacitance with a retention of 95 % after 10,000 cycles [13]. Though having excellent supercapacitor performance, industrial scaling for bulk electrode powder production is challenging. Electrodeposited films also exhibit poor repeatability due to sensitivity to deposition parameters [14]. Another widely used method is calcinating oxides of transition metals in ammonia atmosphere. Corn shaped TiN electrodes with excellent pseudocapacitance were synthesized by annealing TiO_2 shell in ammonia atmosphere [15]. The specific morphology helped it to achieve a high specific capacitance of 20.7 F cm^{-3} at 1 V s^{-1}. Recently, Zhou et al. synthesized TiN based ZnO nanoparticles for supercapacitor applications [16]. TiN nanobuds were synthesized from TiO_2 by annealing in ammonia atmosphere. This synthesis route enables bulk production of TiN powder; however, it relies on ammonia, a hazardous gas. Recently, there have been reports discussing strategies in which ammonia for nitridation is generated in-situ within the reaction chamber, thereby mitigating safety concerns [17]. Guo et al. used melamine as the nitridation agent in the synthesis of TiN/C, which exhibit high specific capacitance [18].

In recent studies, MXene is being used as a potential precursor, for its morphological advantages and chemical properties [19,20]. Park et al. produced vertically aligned TiO_2 by laser irradiation on MXene/Graphene composite [21]. Similarly, porous nitrogen-doped C/TiO_2 derived from PANI/MXene composite was demonstrated to have excellent supercapacitor behavior and EMI shielding [22]. Urbenkowski et.al reported the synthesis of transition metal nitrides like V_2N and Mo_2N by ammoniation of carbide MXenes at high temperature, where replacement of carbon with nitrogen led to metallic conductivity over semiconductor conductivity of parent carbides [23]. 2D TiN-C sheets have been proved to be an efficient polysulfide trap for Li—S batteries consequently improving its cycling stability. These sheets were prepared by sintering Ti_3C_2 MXene in an ammonia atmosphere [24].

Here a new synthesis route is proposed where Ti_2C MXene is used as the primary precursor for TiN synthesis. A mixture of Ti_2C, urea, PEG 2000 and boric acid is annealed to obtain TiN decorated with carbon agglomerations. The synthesis procedure is illustrated in Fig. 1 (a). The accordion structure of MXene is retained in the synthesized TiN, enabling high effective surface area for electrode-electrolyte interaction. Ammonia for nitridation is in-situ generated by urea. PEG 2000 brings agglomerated carbon networks on the TiN structure, and improves the morphological and electrochemical aspects of the material. PEG generates reactive oxygen species (ROS) when annealed at high temperature, leading to undesirable oxidized residues in the product. The role of boric acid is to prevent this oxidation. Role of each component in the precursor mixture is understood from the comparative study of XRD and XPS analysis of the synthesized TiN, Ti_2C-NC and Ti_2C-N. Ti_2C-NC is prepared by annealing Ti_2C with urea and PEG, while Ti_2C-N is prepared by annealing Ti_2C with urea alone. Ti_2C-900 sample is prepared by annealing Ti_2C alone in the same conditions. To meet the growing demand for miniaturized energy storage, a microsupercapacitor device was fabricated using the synthesized TiN material. Its compact design and small footprint make it well-suited for integration into various applications, particularly in microelectronics. The practical applicability of the device is demonstrated by powering an LED using four microsupercapacitors connected in series.

2. Material synthesis

The detailed synthesis processes of Ti_2C, Ti_2C-900, Ti_2C-N, Ti_2C-NC, and TiN materials are as follows: At first, Ti_2C was synthesized by selective acid etching of Ti_2AlC MAX phase using LiF and HCl. In 20 mL of

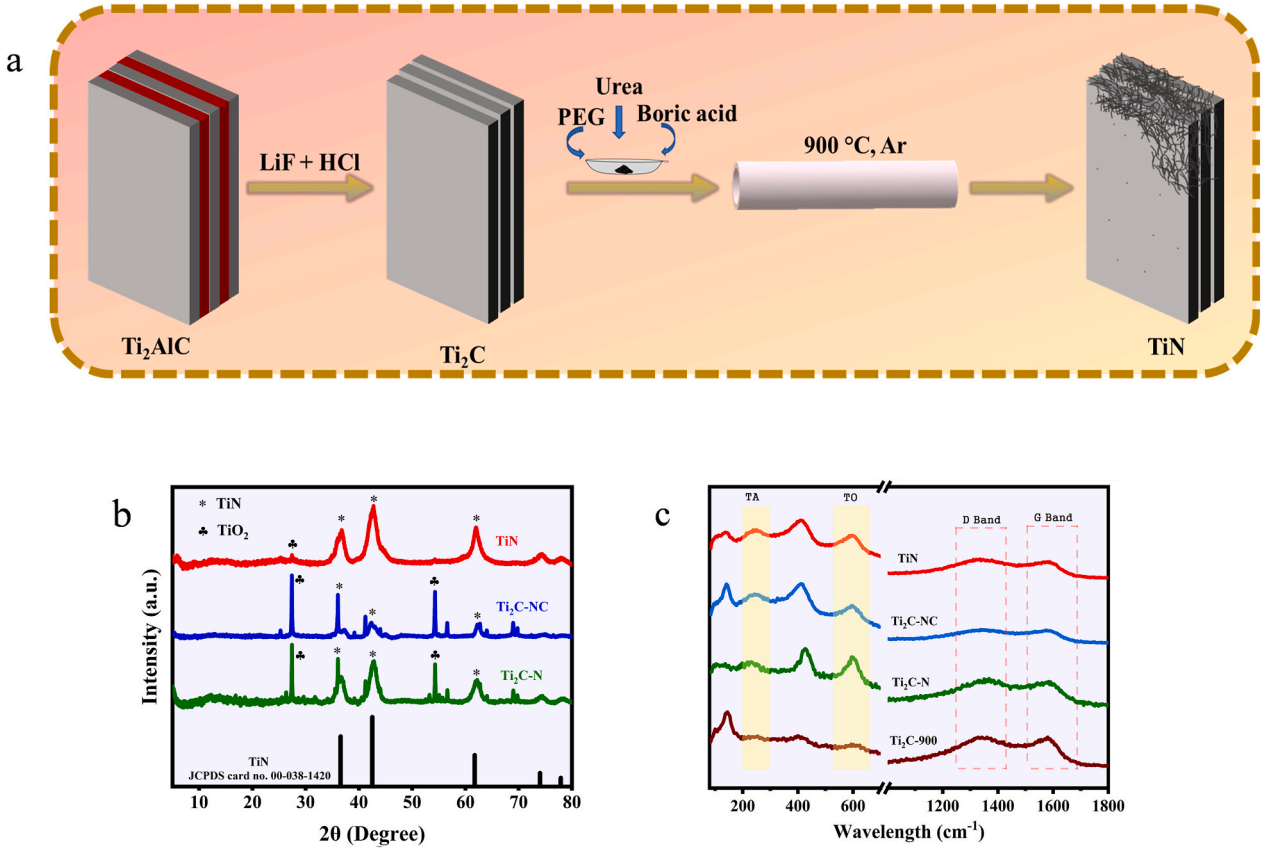

Fig. 1. (a) Schematic diagram of TiN synthesis, (b) XRD and (c) Raman spectra of Ti_2C-900, Ti_2C-N, Ti_2C-NC, and TiN materials.

9 M HCl, 1 g of LiF was dissolved, followed by the slow addition of 1 g of Ti_2AlC MAX phase. The mixture was stirred at 40 °C for 48 h. After etching, the solution was repeatedly washed with deionized water by centrifugation at 6000 rpm until the pH of the supernatant exceeded 6. The resulting sediment is then freeze-dried to obtain etched Ti_2C material. The resultant Ti_2C material was annealed at 550 °C for 4 h and then at 900 °C for 1 h in argon atmosphere to obtain the Ti_2C-900 material. The same annealing procedure was also used to prepare Ti_2C-N, Ti_2C-NC, and TiN materials. The Ti_2C-N material was synthesized by mixing and grinding 200 mg of Ti_2C with 400 mg of urea, followed by the annealing process. For the preparation of Ti_2C-NC material, 5.5 g of urea was dissolved in 1 g of PEG (dissolved in 100 mL of water) and dried in a hot air oven at 120 °C for 14 h. 400 mg of obtained mixture was ground with 200 mg of Ti_2C for 30 min and then annealed to get the Ti_2C-NC material. For the preparation of TiN material, 1 g PEG 2000 and 0.15 g boric acid were dissolved in 100 mL of DI water. After that, 5.5 g of urea was added to the abovementioned solution mixture and dried in a hot air oven at 120 °C for 14 h. A 400 mg of dried material was thoroughly ground with Ti_2C (200 mg) and then annealed to obtain the TiN material. Fig. 1 (a) demonstrates the synthesis process of TiN material. The material, characterization techniques, electrode preparation, and micro supercapacitors fabrication processes were provided in the SI sections (1–4).

3. Results and discussion

Fig. 1(b) shows the XRD patterns of the Ti_2C-N, Ti_2C-NC, and TiN materials. All materials have XRD peaks around 37°, 42°, 62°, 74°, and 78°, which correspond to (111), (200), (220), (311), and (222) crystal planes, respectively. XRD pattern of material TiN aligns with JCPDS card no. 96–900-1628. The oxide peaks present in Ti_2C-N and Ti_2C-NC belongs to rutile TiO_2 (JCPDS card no. 96–900-1682). Since Ti—N and Ti—C exhibit characteristic peaks at similar positions, their compositions cannot be accurately distinguished using XRD analysis alone. Dominant species in the sample is further confirmed by subsequent XPS analysis. It is observed that the diffraction peak intensity of the Ti_2C-NC material is lower compared to that of the Ti_2C-N material. This is attributed to the presence of the PEG source, which promotes greater TiO_2 formation over TiN material. The XRD pattern of TiN exhibits more prominent TiN peaks compared to those of the oxidized products. This is due to the introduction of boric acid during the synthesis process. This is explained as follows: At first, two moles of boric acid (H_3BO_3) are converted into two moles of HBO_2 during the annealing process. Subsequently, during the continued annealing process, HBO_2 is thermally converted into B_2O_3 [25,26]. Previous studies have shown that boron oxide or boric acid can act as reducing agents for graphene oxide [27,28]. In such cases, these boron-containing compounds help suppress oxidation by donating electrons or forming barrier layers. Similarly, in the present work, boron oxide or boric acid reduces the extent of oxidation during the annealing process, thereby minimizing the formation of oxidized products. The formation of B_2O_3 is further confirmed using the XPS analysis. The XRD pattern of Ti_2AlC and Ti_2C (Fig. S1) confirms the successful etching of the Ti_2AlC MAX phase. Additionally, the XRD pattern of Ti_2C-900 (Fig. S1) displays a combination of Ti—C and oxide peaks, as expected for a MXene phase annealed at elevated temperatures.

The Raman spectra (Fig. 1 (c)) of the Ti_2C-900, Ti_2C-N, Ti_2C-NC, and TiN materials show the bands at 253, 412, and 596 cm^{-1}, due to the presence of nonstoichiometric titanium carbide material [29]. The band at 140 cm^{-1} is due to the anatase phase of TiO_2 material. The bands at

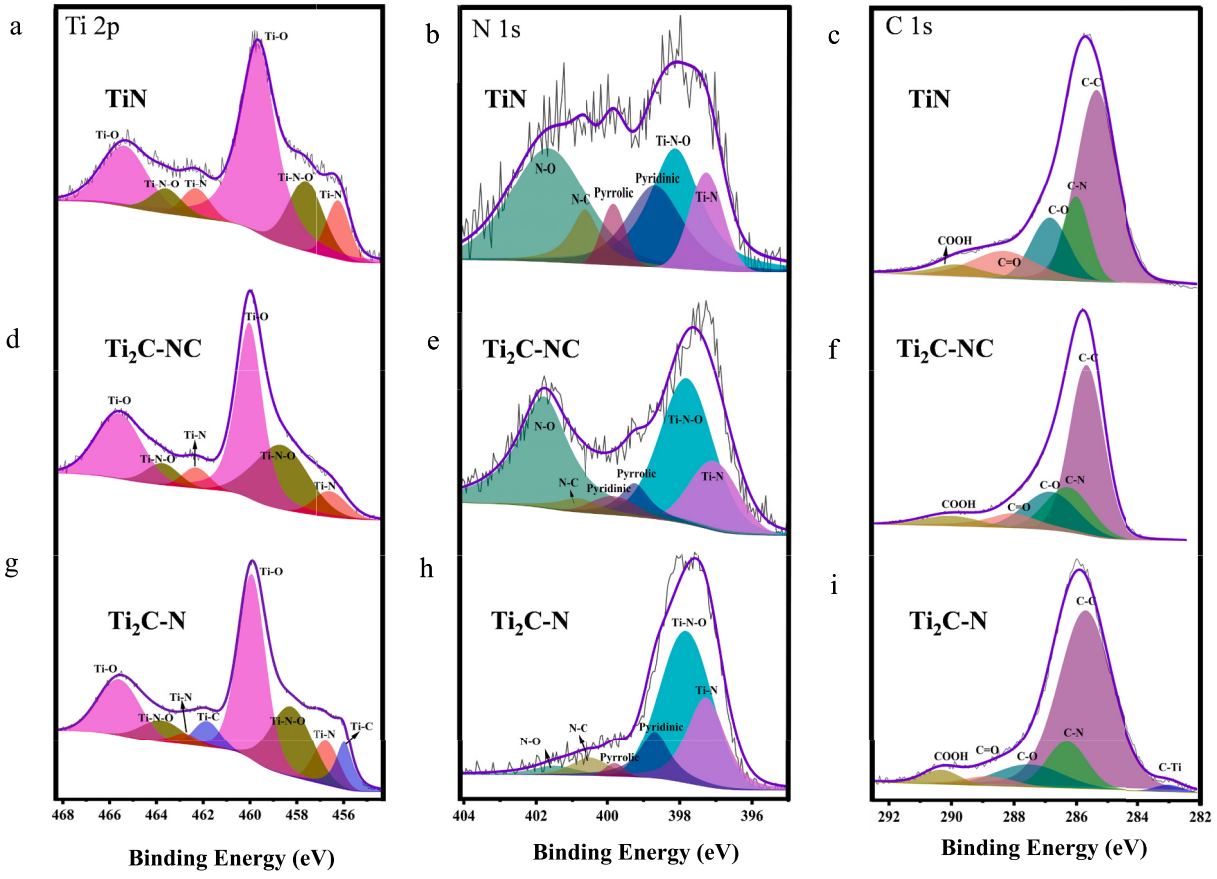

Fig. 2. (a, b, c) Ti 2p, N 1 s and C 1 s XPS spectra of TiN material; (d, e, f) Ti 2p, N 1 s and C 1 s XPS spectra of Ti_2C-NC material respectively; (g, h, i) Ti 2p, N 1 s and C 1 s XPS spectra of Ti_2C-N material respectively.

238, 432, and 609 cm^{-1} correspond to the occurrence of the rutile TiO_2 phase [30]. The bands at 1332 and 1574 cm^{-1} are due to the D and G bands of carbon materials [31]. The obtained results validate the XRD analysis.

The XPS analyses were performed on Ti_2C-N, Ti_2C-NC, and TiN samples to evaluate their oxidation states (Fig. 2). Fig. S2 (a-c) presents the survey spectra of all the materials, clearly showing the presence of Ti, N, and C peaks, thereby confirming the successful formation of the respective compounds. Additionally, the survey spectrum of the TiN material shows the presence of a boron peak, which is a result of the boric acid utilization during the synthesis process. Deconvoluted B1s spectrum (Fig. S2 d) further confirms B_2O_3 in the TiN material.

Ti 2p comparison: Fig. 2 (a, d, g) represents Ti 2p XPS spectra of TiN, Ti_2C-NC, Ti_2C-N samples respectively. Deconvolution of Ti 2p XPS spectra of TiN shows six peaks. Ti ½ states of Ti—N, Ti-N-O and Ti—O are at 456.2 eV, 457.6 eV and 459.7 eV respectively, while the Ti 3/2 states of the corresponding peaks lie at 462.3 eV, 463.6 eV and 465.4 eV. The peak positions of the aforementioned bands for Ti_2C-NC and Ti_2C-N are at nearly same positions. In addition to those peaks, XPS spectra of Ti_2C-N shows Ti—C peaks at 456 eV (Ti 2p 1/2) and 461.8 eV (Ti 2p 3/2) indicating the strong presence of TiC in the material. Notably, Ti 2p ½ Ti—N peak in TiN sample is more intense than the corresponding peak in Ti_2C-NC sample, denoting better stoichiometry and lesser disorder [32]. The reason for high intense Ti—N peak is the oxidation inhibiting property of boric acid under annealing. Boric acid, under high temperature (~500 °C) decomposes into B_2O_3 and acts as an oxidation inhibitor. It is reported that at elevated temperatures, boric acid transforms into a glassy liquid that coats the material surface, thereby preventing further oxidation [33]. Thus, under a well-defined chemical environment, more of nitrate species from urea decomposition reacts with Ti giving a predominant TiN phase.

N1s comparison: Fig. 2 (b, e, h) shows N 1 s spectra of samples TiN, Ti_2C-NC and Ti_2C-N respectively. Deconvolution of the spectra of TiN (Fig. 2 b) gives Ti—N, Ti-N-O, Pyridinic N, Pyrrolic N, N—C and N—O peaks at 397.3, 398.1, 398.7, 399.8, 400.6 and 401.7 eV respectively. Corresponding peaks for the N 1 s spectra of Ti_2C-NC and Ti_2C-N are at nearly same positions. But, a remarkable change in the peak width is observed for N—C bond and N—O bond. Nitrogen-oxygen peak of Ti_2C-N is barely detectable while other two materials show broad and intense N—O peaks. PEG upon annealing undergoes oxidative degradation causing release of reactive oxygen species, which readily reacts with nitrogen from urea and gives nitrate groups [34]. This is the reason for the broad and intense N—O peak of Ti_2C-NC when compared to Ti_2C-N. Similarly, nitrogen-carbon peak of TiN is significantly intense than that of sample Ti_2C-NC and Ti_2C-N. This remarkable change is also due to the presence of boric acid in the TiN precursor. As more nitrate species is caused to react with the carbon species instead of oxygen, N—C peak intensity increases and N—O peak intensity decreases w.r.t Ti—N peak. The less intense Ti-N-O peak w.r.t Ti—N peak for TiN sample when compared to that of Ti_2C-NC, also suggests the oxidation inhibiting effect of boric acid.

C1s comparison: Fig. 2 (c, f, i) depicts the deconvoluted C1s spectra of TiN, Ti_2C-NC and Ti_2C-N respectively. A peak at 283 eV, corresponding to C—Ti bond is present in Ti_2C-N and not in the other two materials, confirming that the predominant phase is TiN. For TiN, C—C peak is shifted to lower BE (285.35 eV) when compared to that of Ti_2C-NC (285.65 eV) and Ti_2C-N (285.7 eV). The shift in peak position is due to the change in oxidation conditions during annealing process, under the influence of boric acid [35,36].

Fig. S3 (a, b) presents the morphological characterization of Ti_2C-900, revealing a layered accordion structure. It is evident that MXene sheets create a particular network of slit-shaped pores that are joined by particular bridges to support the stacked structure. The smooth surface of MXenes sheets is visible in a higher magnification SEM image. Fig. 3 (a, b) shows the morphological analysis of the Ti_2C-N material, which displays a rough surface with a closed layer structure similar to MXene sheets. This morphology is predominantly governed by the annealing process carried. During annealing, urea decomposes and releases gases such as NH_3 and CO_2, which can intercalate between the MXene layers. This process temporarily increases the interlayer spacing and facilitates the partial exfoliation or expansion of the nanosheets. As the temperature rises, urea further decomposes, contributing nitrogen species that promote surface modification and doping. Eventually, the gaseous byproducts escape, leading the layers to restack, but now with altered surface chemistry and increased roughness. Fig. 3 (c, d) shows the SEM images of the Ti_2C-NC material, which exhibits an aggregated structure. This morphology is attributed to the use of PEG during synthesis, which facilitates the formation of a uniform carbon layer enriched that fully coats the surface of the Ti_2C sheets. In addition, the level of oxidation during annealing can lead to a complete change in morphology and restacking of sheets as reported by Alshareef et al. [37]. Fig. 3 (e, f) presents the SEM images of the TiN material, revealing that the characteristic accordion-like structure of the parent MXene is well preserved after its transformation into TiN. This retained structure, along with its

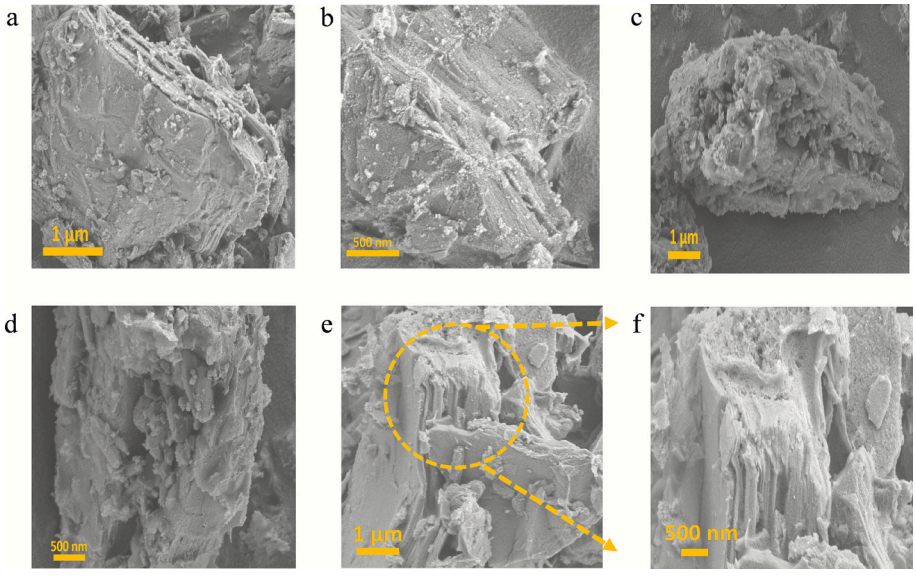

Fig. 3. HR-SEM images of (a-b) Ti_2C-N, (c-d) Ti_2C-NC, (e-f) TiN materials.

inherent porosity, greatly enhances the available surface area for electrode–electrolyte interactions, which is beneficial for electrochemical performance.

The morphological features of the TiN material were further examined using TEM analysis. As shown in Fig. 4(a), the TiN exhibits a sheet-like structure, confirming the preservation of its layered morphology. The TEM lattice fringes shown in Fig. 4 (b, c) reveal interplanar spacings of 0.15 nm and 0.21 nm, corresponding to the (220) and (200) planes, respectively. These values are in good agreement with the TiN phase identified in the XRD pattern, as referenced by JCPDS card no 00–038-1420. The spot angle measurement using GATAN software reveals a d-spacing of 0.33 nm, which corresponds to the negligibly small TiO_2 peak at 27° observed in the XRD pattern (Fig. S5). This matches well with the characteristic peak of rutile-phase TiO_2. The selected area electron diffraction (SAED) pattern of TiN (Fig. 4(d)) displays distinct bright spots, confirming the polycrystalline nature of the material. The elemental mapping (Fig. 4(e)) confirm the existence of Ti, N, C, B, and O elements in the TiN sample. These results agree with the results from the XRD and XPS analyses.

4. Electrochemical analysis

The Ti_2C-900, Ti_2C-N, Ti_2C-NC, and TiN electrodes were electrochemically characterized comprehensively using a standard three-electrode system in 1 M Na_2SO_4 electrolyte.

The cyclic voltammetric (CV) studies of all electrodes were done in the potential limits ranging from −0.3 V and 0.8 V, utilizing diverse scan rates from 10 to 100 mV s^{-1}. The CV curves of all electrode materials, recorded at 100 mV s^{-1} (Fig. 5(a)), display nearly rectangular shape characteristics with no noticeable redox peaks, demonstrating the EDLC behavior. Furthermore, the wide potential window (1.1 V) of the CV curves indicates high energy density and excellent supercapacitor performance. Among the studied materials, the TiN electrode exhibits a significantly larger area under the CV curve, indicating higher charge storage capability. The CV curves of Ti_2C-900, Ti_2C-N, Ti_2C-NC, and TiN electrodes with increasing scan rates are shown in Fig. S6 (a-c) and Fig. 5 (b), respectively. Based on the consistent shape and pattern of the CV curves, the electrodes were stable within their stated voltage range at lower to higher scan rates. It is noteworthy that a clear increase in current with increasing scan rates suggests that the electrodes have ideal capacitive behavior for rapid charge and discharge, making the materials a viable option for electrochemical capacitors.

Evaluating the charge storage kinetics is a significant factor for the supercapacitor, which is calculated using Eq. (1):

$$log\,(i) = b\log\,(v) + \log a \tag{1}$$

where, v is the scan rate (mV s^{-1}) and i is the peak current (A). The slope of the curve b can be found by plotting $log\ v$ versus $log\ i$. A b value near 0.5 signifies a diffusion-controlled capacitive process, whereas a b value close to 1 suggests a surface-controlled capacitive process. Fig. 5 (c) demonstrates that the anodic b values for the Ti_2C-900, Ti_2C-N, Ti_2C-NC, and TiN electrodes are 0.67, 0.43, 0.86, and 0.78, respectively, while the corresponding cathodic b values are 0.54, 0.47, 0.74, and 0.75. Due to the intermediate b-values, the kinetic evolution of the electrode is further quantified by the Eq. (2)

$$i = k_1 v + k_2 v^{1/2} \tag{2}$$

where the $k_1 v$ denotes the surface-controlled contribution and $k_2 v^{1/2}$ is the diffusion-controlled capacitive contribution process. Fig. S6 (d) and Fig. 5 (d) show the surface and diffusion-controlled contributions of Ti_2C-900, Ti_2C-N, Ti_2C-NC, and TiN electrodes at a scan rate of 20 mV s^{-1}. The Ti_2C-900, Ti_2C-N, Ti_2C-NC, and TiN electrodes reveal the surface-controlled process of 15.5 %, 7.9 %, 34.6 % and 26.3 % respectively, whereas the diffusion-controlled process of 84.5 %, 92.1 %, 65.4 % and 73.7 % respectively. It is clear that a diffusion-controlled energy storage process accounts for the majority of the charge stored by all electrodes. Fig. 5 (e) demonstrates the surface and diffusion-controlled contribution of the TiN material at all scan rates. The dominant diffusion contribution is attributed to the reversible intercalation and deintercalation of Na^+ ions within the TiN interlayers. The sheet-like, accordion-type morphology of TiN provides ion diffusion pathways while maintaining structural integrity during cycling. It shows that as the scan rate is increased from 20 to 100 mV s^{-1}, the diffusion-controlled process tends to decrease, which is due to the time restrictions at high scan rates. Slower scan rates improve battery-type capacitive behavior by giving electrolyte ions more time to infiltrate into the interior pores of TiN layers and participate in Faradaic reactions. Higher scan rates prevent the ions from completely entering the interior pores due to the limited time. This results in a larger contribution from the surface-controlled process at high scan rates [38].

The galvanostatic charge/discharge (GCD) analysis was done for Ti_2C-900, Ti_2C-N, Ti_2C-NC, and TiN electrodes at a current density of 3 mA cm^{-2}, as shown in Fig. 5 (f). All GCD profiles have symmetric charge-discharge curves, which suggests that the electrode materials have outstanding reversibility. The occurrence of a triangular profile in the GCD curves supports the EDLC property and is better associated with CV analysis. Fig. 5 (g) shows the GCD analysis of the TiN electrode, recorded using 3, 4, and 5 mA cm^{-2}.

The areal capacitance of the materials is calculated using Eq. (3).

$$C_s = \frac{I \times \Delta t}{A \times V} \tag{3}$$

where I is the current, Δt is the discharge time, A is the area of the

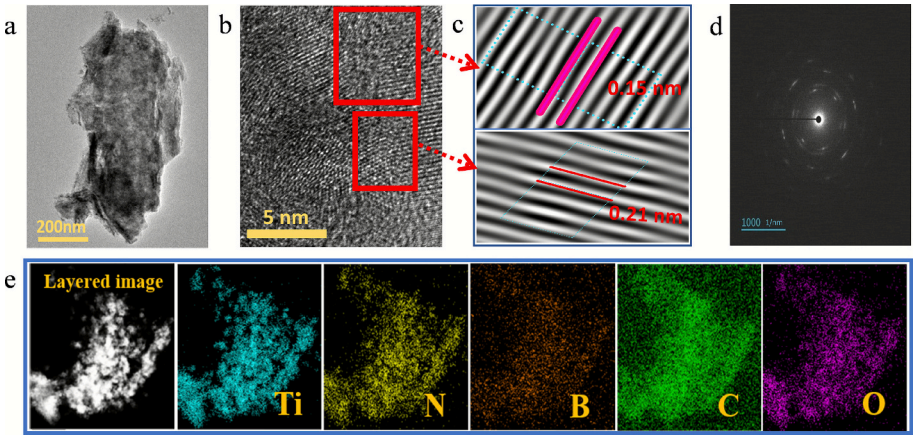

Fig. 4. TEM analyses of TiN material (a) TEM image, (b) HR-TEM, (c) fringes, (d) SAED pattern, and (e) EDS mapping analysis.

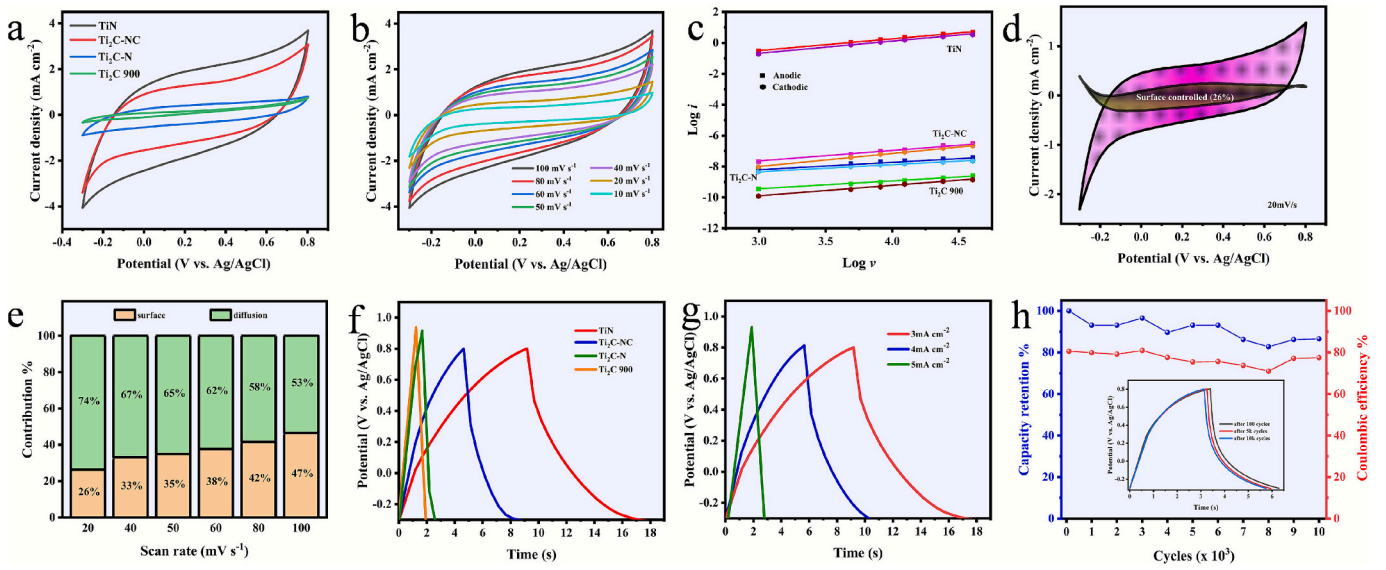

Fig. 5. Three electrode electrochemical measurements of Ti₂C-900, Ti_2C-N, Ti_2C-NC, and TiN electrodes: (a) CV curves of all electrodes at 100 mV s^{-1}, (b) CV curves of TiN at different scan rates, (c) log i vs. log v graph, (d) diffusion contribution of TiN electrode at 20 mV s^{-1}, (e) capacitive and diffusion contribution of TiN electrode at different scan rates, (f) GCD curves of all electrodes, (g) GCD curves of TiN at different current density, (h) cycling stability and coulombic efficiency of TiN electrode.

electrode, and V is the voltage window. The Ti_2C-900, Ti_2C-N, Ti_2C-NC, and TiN electrodes exhibit the areal capacitance of 0.71 mF cm^{-2}, 2.6 mF cm^{-2}, 11.04 mF cm^{-2} and 23.26 mF cm^{-2}, respectively, at 3 mA cm^{-2}. Among the tested electrodes, the TiN electrode has the highest areal capacitance, comparable to previous reports mentioned in Table 1.

The superior supercapacitor performance of TiN is attributed to its accordion-like structure, which enhances surface area and ion diffusion. Additionally, its high electrical conductivity facilitates rapid electron transport while maintaining its structural stability. The higher concentration of surface functional groups, such as C—O and C═O, in the TiN electrode enhances its capacitive performance [44]. Additionally, the presence of pyridinic-N and pyrrolic-N species further contributes to efficient charge storage, as these nitrogen functionalities are known to promote capacitive behavior [45,46]. The TiN electrode was subjected to 10,000 charge-discharge cycles at 4 mA cm^{-2} to evaluate its long-term electrochemical durability (Fig. 5 (h)). The inset of Fig. 5 (h) shows the 100th, 5000th, and 10000th GCD cycles of the cyclic stability test. After 10,000 GCD cycles, the material maintained 84 % of its initial capacitance and 95.4 % coulombic efficiency (Eq. S1). TiN electrode shows exceptional electrochemical stability due to strong mechanical structure and good conductivity. Reversible ion adsorption is improved by stable oxygen-containing surface groups (C—O, C═O) [47].

The electrochemical impedance spectroscopic studies were done for the TiN electrode in a symmetric coin cell assembly before and after 50 consecutive CV curves at 10 mV s^{-1}, as shown in Fig. S7 (a). Corresponding equivalent circuit with three branches is also given as Fig. S7 (b, c) [48]. The series resistance R_s represents the total ohmic contribution from the electrolyte, current collector, and contact interfaces, determined from the high-frequency intercept of the Nyquist plot. Prior to cycling, R_s is 1.35 Ω, increasing slightly to 1.60 Ω after cycling; however, both values remain sufficiently low to ensure good overall conductivity. The first R||Q branch is associated with interfacial charge-transfer processes occurring at the electrode–electrolyte interface [49]. The constant phase element reflects non-ideal capacitive behavior attributed to surface roughness and the porous nature of the TiN film [50]. Initially, the large resistance in this branch indicates the presence of a native TiO_x surface layer that restricts charge transfer. After 50 cycles, the significant reduction in this resistance suggests that the surface becomes more electrochemically active, thereby enhancing interfacial reaction kinetics. The second R||Q branch corresponds to ion diffusion and charge storage within the porous TiN structure. Before cycling, the low resistance and small exponent value ($n = 0$) indicate a highly porous electrode with deep ion penetration into subsurface regions [51]. Following cycling, an increase in n value toward unity reflects more ideal capacitive behavior, signifying the activation of internal pores and improved electrochemical utilization of the electrode. Finally, the capacitor in the third branch represents the ideal double-layer capacitance dominant in the low-frequency region, where charge storage is primarily capacitive in nature.

Na-ion diffusion coefficient of the material is calculated using the Eq. (4).

$$D_{Na} = \frac{R^2T^2}{2\sigma_w^2 c^2 F^4 n^4 A^4} \quad (4)$$

where D_{Na} represents the sodium ion diffusion coefficient. R, T, A, n, F and c in the equation are the gas constant, absolute temperature, effective area of the electrode, number of electrons transferred, faraday constant and concentration of sodium ion respectively. The Warburg impedance coefficient σ_w could be determined from the slope between Z_{re} and $\omega^{-1/2}$ as shown in Fig. S7 (d). From the Eq. (4), diffusion coefficient is calculated to be 8.15×10^{-11} cm^2 s^{-1}.

In situ Raman spectroscopy was conducted during CV over 0–1 V (vs.

Table 1
Performance comparison with previous works.

S. No	Material	Performance	Electrolyte	Ref.
1	TiN-S	15 mF cm^{-2} at 5 mV s^{-1}	1 M KOH	[39]
2	TiVN	15 mF cm^{-2} at 2 mV s^{-1}	1 M KOH	[40]
3	TiN	12 mF cm^{-2} at 2 mV s^{-1}	0.5 M K_2SO_4	[41]
4	TiN/VG (vertical graphene)	9 mF cm^{-2} at 100 mV s^{-1}	1 M Li_2SO_4	[42]
5	CrN	12.8 mF cm^{-2} at 1 mA cm^{-2}	0.5 M H_2SO_4	[43]
6	VN	19 mF cm^{-2}	1 M KOH	[43]
7	**TiN**	**23.3 mF cm^{-2}**	**1 M Na_2SO_4**	**This work**

Ag/AgCl) in 1 M Na_2SO_4 using a symmetric coin cell at room temperature (Fig. S8 (a, b)). The spectra display two Raman peaks at ~453 cm^{-1} and ~ 612 cm^{-1}, corresponding to the titanium-oxygen vibration band, indicating the Ti-O-N formation due to surface hydration and oxidation. These surface transformations modify vibrational modes without inducing notable spectral changes between anodic and cathodic scans, indicating the absence of redox activity or structural rearrangement during cycling [52]. From a supercapacitor perspective, the combination of TiN with a conductive core and stable surface oxide layer ensures efficient charge transfer, enhanced electrolyte interaction, and excellent cycling durability, making it a promising candidate for high rate-capability, long-life energy storage systems.

5. Microsupercapacitor studies

A microsupercapacitor (MSC) device (TiN//Na_2SO_4//TiN) has been fabricated with the synthesized TiN, as shown in the schematic diagram (Fig. 6 (a, b)). The fabricated solid-state microsupercapacitor operates within a voltage window of 0 to 1.2 V. As shown in the cyclic voltammetry curves (Fig. 6 (d)), the TiN//Na_2SO_4//TiN device retains a quasi-rectangular shape across the scan rate range of 10 to 100 mV s^{-1}, representing admirable electrochemical stability and good compatibility

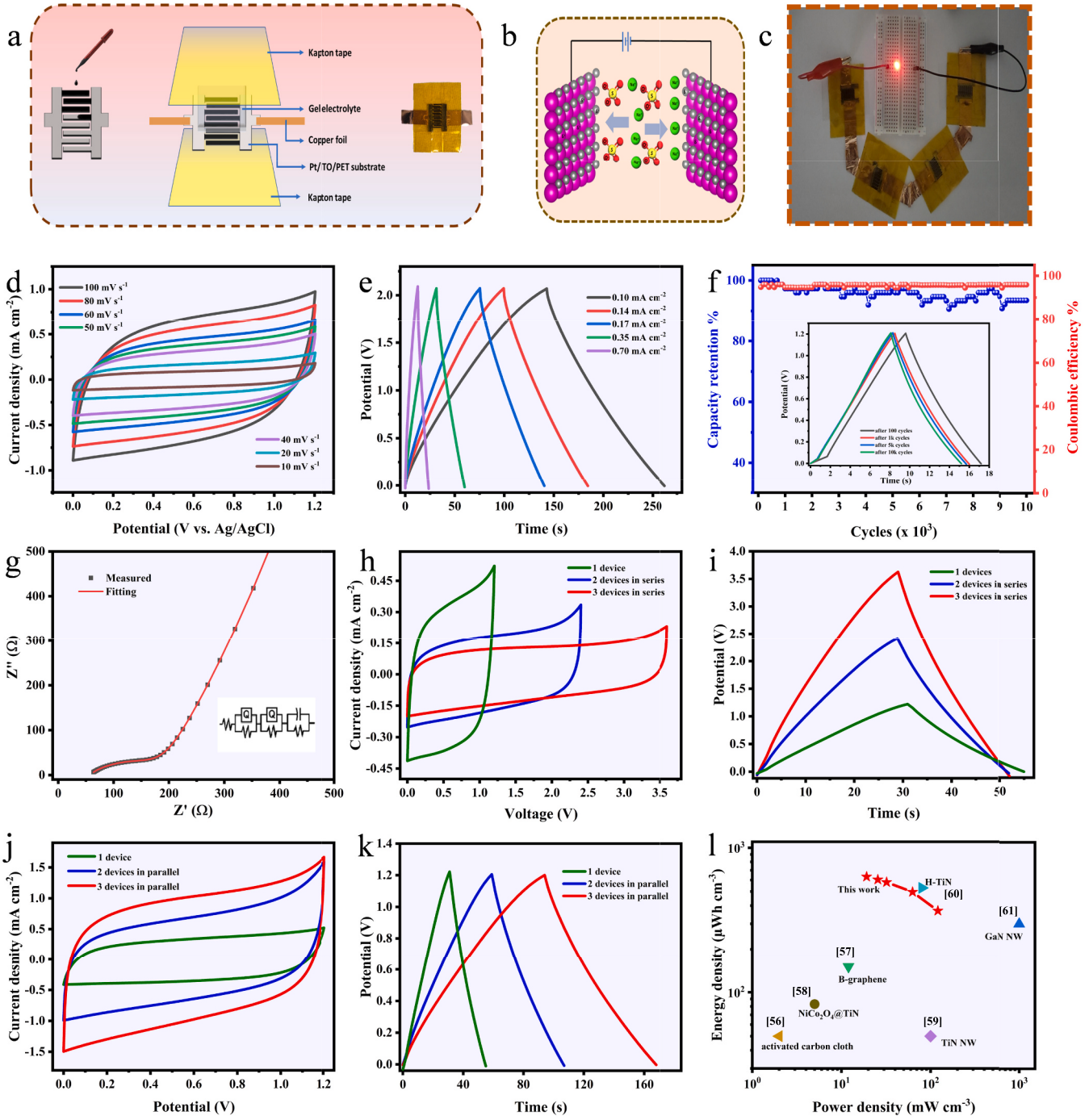

Fig. 6. Device studies: (a) schematic diagram of MSC device fabrication, (b) Schematic diagram of charging of symmetric TiN supercapacitor, (c) digital image of LED lighting with device in series assembly, (d) CV curves, (e) GCD studies, (f) cycling stability studies, (g) EIS measurement, (h) CV curves in series assembly, (i) GCD curves in series assembly, (j) CV curves in parallel connection, (j) GCD curves in parallel connection, and (j) Ragone plot.

between the electrode and electrolyte. Rapid ion transport kinetics and electrochemical reversibility are confirmed by a nearly triangular charge-discharge curve that resembles an ideal supercapacitor. Furthermore, the rectangular shape of CV curves suggests that the charge storage process mostly involves EDLC. Using Eqs. (1) and (2), the surface-controlled and diffusion-controlled processes were determined for the microsupercapacitor, as shown in Fig. S9 (a). The capacitive contribution is calculated to be 64 % at a scan rate of 20 mV s^{-1} and increases to 80 % at 100 mV s^{-1}. Fig. 6 (e) shows the GCD analysis of the microsupercapacitor with various current density values. All GCD curves establish a triangular profile, indicating the EDLC-type, which is consistent with the results found from the CV studies. The device offers an aerial capacity of 10.3 mF cm^{-2} at 0.1 mA cm^{-2} current density, and shows an acceptable rate capability of 61 % at a high current density of 0.7 mA cm^{-2} (Fig. S9 (b)). A comparison table of the fabricated TiN MSC with a few other reported MXene based MSC devices is given in Table S1. The device underwent 10,000 GCD cycles at a current density of 0.7 mA cm^{-2} to assess the cycling stability (Fig. 6 (f)) of the TiN//Na_2SO_4//TiN microsupercapacitor. The inset of Fig. 6 (f) shows the 100th, 1000th, 5000th and 10000th cycles of cyclic stability analysis. After 10,000 cycles, the results show a remarkable 95.8 % coulombic efficiency and 92 % capacity retention, indicating its great promise for useful, application-focused systems. Electrochemical impedance spectrum is given in Fig. 6 (g) and the equivalent circuit model is similar to that of TiN electrodes in coin cell assembly. The device shows a solution resistance (R_s) of 55.7 Ω and charge transfer resistance (R_{ct}) of 155.5 Ω, which is ahead of some of the reported works [53–55].

To address the potential need for combining multiple MSCs in practical applications, the electrochemical performance of series and parallel configurations was investigated. For this purpose, two and three microsupercapacitor devices were connected in both series and parallel arrangements. In the CV curves of series configuration (Fig. 6 (h)), three connected devices exhibit an extended operating voltage window of 3.6 V, while two devices reach 2.4 V. Notably, the GCD curve (Fig. 6 (i)) durations of both combinations closely match that of a single device, indicating efficient voltage scaling without compromising charge–discharge behavior. In the parallel configuration (Fig. 6 (j)), the operating voltage window remains fixed at 1.2 V. As observed in the CV curves, there is a gradual increase in the overall CV area, indicating enhanced charge storage. This is further supported by the GCD curves in Fig. 6 (k), which show a linear increase in charge–discharge time with additional devices.

Energy density and power density of the device is calculated using the following equations:

$$\text{Energy density}, E_d = \frac{I}{A}\int V.dt \tag{5}$$

where, $\int V.dt$ is the time integration over the discharge curve is GCD

$$\text{Power density}, P_d = \frac{E_d}{t_d} \tag{6}$$

where, t_d is the discharge time.

The microsupercapacitor shows maximum energy density of 632 μWh cm^{-3} at a power density of 19 mW cm^{-3}. Ragone plot in Fig. 6 (l) shows the energy density of the device at different power densities and it is substantially higher than the other reported supercapacitors, such as carbon based materials like activated carbon cloth (50 μWhcm^{-3} at 2 mW cm^{-3}) [56], boron doped graphene (150 μWh cm^{-3} at 12 mW cm^{-3}) [57], and nitrides like $NiCo_2O_4$@TiN nanofibers (83 μWh cm^{-3} at 5 mW cm^{-3}) [58], TiN NW derived from TiO_2 (50 μWh cm^{-3} at 100 mW cm^{-3}) [59], hierarchical TiN nanoparticles-assembled nanopillars (530 μWh cm^{-3} at 80 mW cm^{-3}) [60] and GaN NW (300 μWh cm^{-3} at 1000 mW cm^{-3}) [61].

To demonstrate the potential for practical applications, a red LED was powered using a series combination of four TiN//Na_2SO_4//TiN devices, as shown in Fig. 6 (c). A video file is provided as supplementary data. The LED remained brightly illuminated for at least 30 s before it began to gradually fade, demonstrating the effective energy delivery capability of the TiN//Na_2SO_4//TiN assembly.

To assess the structural and morphological stability, the TiN slurry was coated onto carbon paper, subjected to 1000 GCD cycles in a 1 M Na_2SO_4 electrolyte for post-cycling characterization. Before and after (Fig. 7 (a, b)) cycling stability test, the XRD investigation shows no discernible changes in the crystalline structure of the TiN material. The outstanding structural stability of the TiN electrode is confirmed by the preservation of the original diffraction peaks corresponding to (111) and (200) planes without any discernible shift, widening, or emergence of new phases. The dominant peak at 26° and 54° belonging to graphitic carbon is from the carbon paper substrate. No noticeable structural changes were observed in the SEM images before (Fig. 7 (c, d)) and after cycling (Fig. 7 (e, f)) test, indicating excellent morphological stability of the TiN electrode. This stability can be attributed to the robust nature of the TiN material and its strong adhesion to the carbon paper substrate, which together help maintain the electrode's integrity during prolonged electrochemical cycling. These results provide strong evidence for the excellent long-term cycling stability of the TiN material.

6. Conclusion

In conclusion, we have synthesized TiN derived from MXene by annealing it with urea, PEG, and boric acid. The effect of each compound on pristine MXene during annealing is examined through four samples synthesized with varying precursor combinations. Urea generates ammonia for the nitridation, while PEG brings amorphous carbon agglomerations and further modifies the MXene surface. The addition of boric acid to the precursor suppresses the undesirable oxidation of the material facilitated by PEG. The accordion structure of the pristine MXene was retained by the synthesized TiN along with a carbon network, modifying its surface, allowing superior electrode-electrolyte interaction. The synthesized TiN was found to be an effective supercapacitor material, demonstrating a specific capacitance of 23 mF cm^{-2} and excellent long-term stability, retaining 84 % of its capacitance after 10,000 cycles. As a demonstration of the materials' suitability for technology-oriented applications, a symmetric microsupercapacitor is fabricated using synthesized TiN as the electrode material. The material exhibits dominant EDLC behavior, delivering a specific capacitance of 10 mF cm^{-2}, excellent cycling stability over 10,000 cycles, with 95 % coulombic efficiency and 92 % capacitance retention. The fabricated device shows notably higher performance with an energy density of 632 μWh cm^{-3} at a power density of 19 mW cm^{-3}, promising its use in energy storage applications. Furthermore, the compatibility of the MSC device in series and parallel configurations was demonstrated with electrochemical measurements. The proposed synthetic strategy not only provides high-performance TiN material for supercapacitor applications but also offers a versatile route for synthesizing transition metal nitrides from various MXenes.

Supplementary data to this article can be found online at https://doi.org/10.1016/j.cej.2025.171811.

CRediT authorship contribution statement

Hafis Hakkeem: Writing – original draft, Methodology, Investigation. **Shridhar Hegde:** Validation, Formal analysis, Data curation. **Erdenebayar Baasanjav:** Visualization, Methodology, Investigation. **Johnbosco Yesuraj:** Software, Conceptualization. **Jae-Kwang Kim:** Resources, Methodology. **Jung Sang Cho:** Writing – review & editing, Resources. **Chandra Sekhar Rout:** Writing – review & editing, Supervision, Conceptualization. **Sang Mun Jeong:** Writing – review & editing, Supervision, Funding acquisition, Conceptualization.

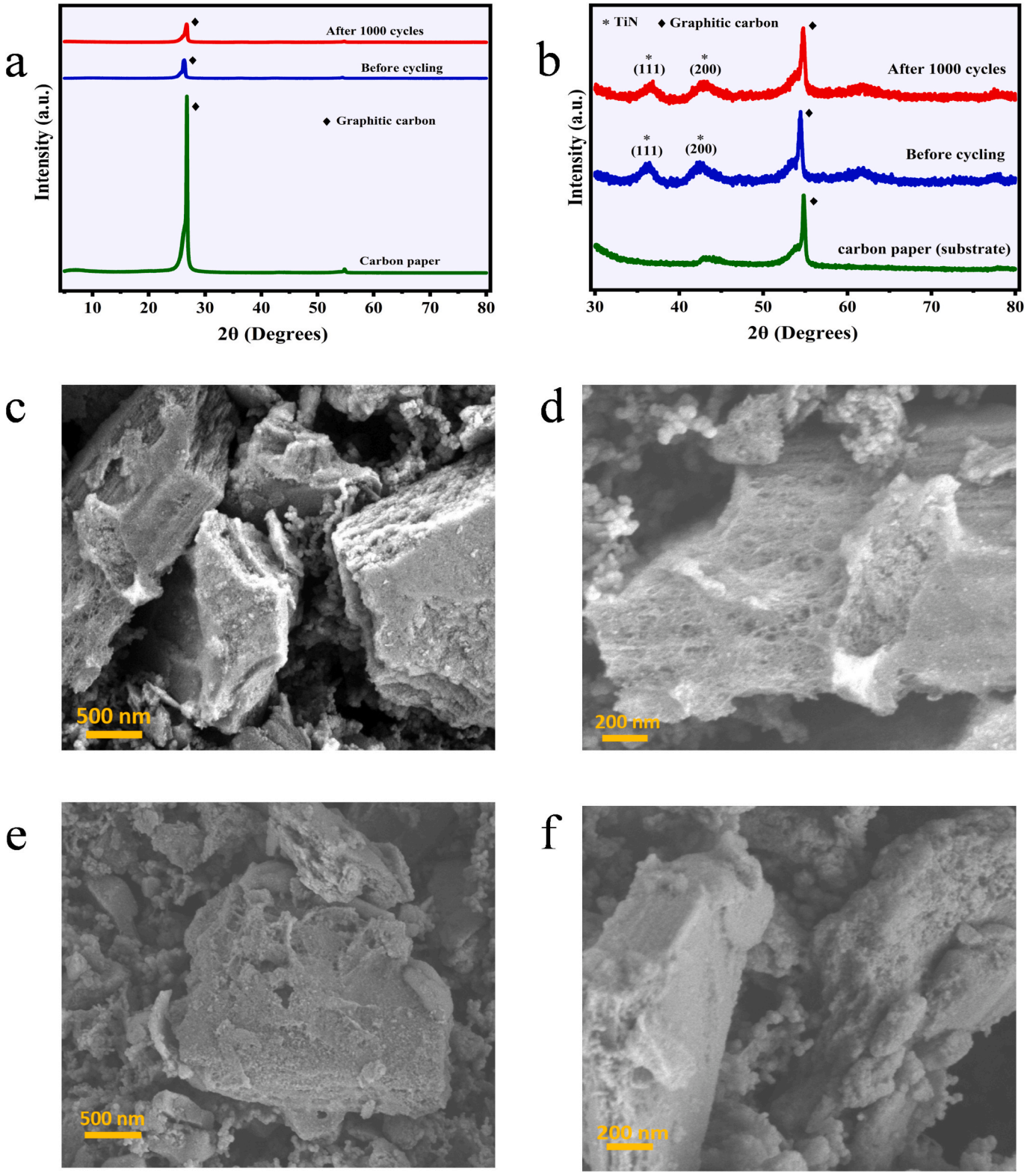

Fig. 7. (a) XRD analysis of TiN electrode before and after continuous 1000 GCD cycles, (b) enlarged spectra of Fig. 7 (a), SEM images of TiN electrode (c-d) before cycling (e-f) after cycling.

Declaration of competing interest

The authors declare the following financial interests/personal relationships which may be considered as potential competing interests: Sang Mun Jeong reports financial support was provided by National Research Foundation of Korea. If there are other authors, they declare that they have no known competing financial interests or personal relationships that could have appeared to influence the work reported in this paper.

Data availability

Data will be made available on request.

Acknowledgement

This work was supported by the National Research Foundation of Korea (NRF) grant funded by the Korea government (MSIT) (No. RS-2024-00345983, RS-2023-00217581) and Regional Innovation System & Education (RISE) program through the Chungbuk Regional Innovation System & Education Center, funded by the Ministry of Education (MOE) and the Chungcheongbuk-do, Republic of Korea (2025-RISE-11-014-03).

References

[1] P. Patsalas, N. Kalfagiannis, S. Kassavetis, G. Abadias, D.V. Bellas, Ch. Lekka, E. Lidorikis, Conductive nitrides: growth principles, optical and electronic properties, and their perspectives in photonics and plasmonics, Mater. Sci. Eng. R Rep. 123 (2018) 1–55, https://doi.org/10.1016/j.mser.2017.11.001.

[2] Z.-G. Yang, H.-M. Xu, T.-Y. Shuai, Q.-N. Zhan, Z.-J. Zhang, K. Huang, C. Dai, G.-R. Li, Recent progress in the synthesis of transition metal nitride catalysts and their applications in electrocatalysis, Nanoscale 15 (2023) 11777–11800, https://doi.org/10.1039/D3NR01607B.

[3] S.A. Shafiee, S.C. Perry, H.H. Hamzah, M.M. Mahat, F.A. Al-lolage, M.Z. Ramli, Recent advances on metal nitride materials as emerging electrochemical sensors: a mini review, Electrochem. Commun. 120 (2020) 106828, https://doi.org/10.1016/j.elecom.2020.106828.

[4] S. Zhang, F. Yan, Y. Yang, M. Yan, Y. Zhang, J. Guo, H. Li, Effects of sputtering gas on microstructure and tribological properties of titanium nitride films, Appl. Surf. Sci. 488 (2019) 61–69, https://doi.org/10.1016/j.apsusc.2019.05.148.

[5] M. Zhang, Y. Lu, Z. Yue, M. Tang, X. Luo, C. Chen, T. Peng, X. Liu, Y. Luo, Design and synthesis of novel pomegranate-like TiN@MXene microspheres as efficient sulfur hosts for advanced lithium sulfur batteries, RSC Adv. 13 (2023) 9322–9332, https://doi.org/10.1039/D3RA00095H.

[6] M. Ahmed, N. Ahmed, H. Ahmad, S. Bashir, R. Subramaniam, G. Ali, A comparative study on exploring sputtered titanium nitride thin films for high-performance supercapacitors, J. Energy Storage 105 (2025) 114712, https://doi.org/10.1016/j.est.2024.114712.

[7] B. Gao, X. Li, K. Ding, C. Huang, Q. Li, P.K. Chu, K. Huo, Recent progress in nanostructured transition metal nitrides for advanced electrochemical energy storage, J. Mater. Chem. A Mater. 7 (2019) 14–37, https://doi.org/10.1039/C8TA05760E.

[8] U. Mahajan, M. Dhonde, K. Sahu, P. Ghosh, P.M. Shirage, Titanium nitride (TiN) as a promising alternative to plasmonic metals: a comprehensive review of synthesis and applications, Mater. Adv. 5 (2024) 846–895, https://doi.org/10.1039/D3MA00965C.

[9] P. Mouchani, R. Sarraf-Mamoory, H. Aghajani, Preparation of titanium nitride/oxynitride nanotube array via ammonia-free PECVD method for enhancing supercapacitor performance, J. Alloys Compd. 904 (2022) 163895, https://doi.org/10.1016/j.jallcom.2022.163895.

[10] J. Shi, B. Jiang, Z. Liu, C. Li, F. Yan, X. Liu, H. Li, C. Yang, D. Dong, J. Hao, Sputtered titanium nitride films on nanowires Si substrate as pseudocapacitive electrode for supercapacitors, Ceram. Int. 47 (2021) 26758–26767, https://doi.org/10.1016/j.ceramint.2021.06.084.

[11] J. Zhao, Y. Zeng, J. Wang, Q. Xu, R. Chen, H. Ni, G.J. Cheng, Ultrahigh electrocatalytic activity with trace amounts of platinum loadings on free-standing mesoporous titanium nitride nanotube arrays for hydrogen evolution reactions, Nanoscale 12 (2020) 15393–15401, https://doi.org/10.1039/D0NR01316A.

[12] Y. Xie, F. Tian, Capacitive performance of molybdenum nitride/titanium nitride nanotube array for supercapacitor, Mater. Sci. Eng. B 215 (2017) 64–70, https://doi.org/10.1016/j.mseb.2016.11.005.

[13] S.A. Ansari, N.A. Khan, Z. Hasan, A.A. Shaikh, F.K. Ferdousi, H.R. Barai, N.S. Lopa, Md.M. Rahman, Electrochemical synthesis of titanium nitride nanoparticles onto titanium foil for electrochemical supercapacitors with ultrafast charge/discharge, Sustain. Energy Fuel 4 (2020) 2480–2490, https://doi.org/10.1039/D0SE00049C.

[14] K. Wandelt, Encyclopedia of Interfacial Chemistry: Surface Science and Electrochemistry. Volume 1, 1.1 Experimental Methods, 1.2 Surface Science Under Environmental Conditions, Elsevier, 2018.

[15] P. Yang, D. Chao, C. Zhu, X. Xia, Y. Zhang, X. Wang, P. Sun, B.K. Tay, Z.X. Shen, W. Mai, H.J. Fan, Ultrafast-charging supercapacitors based on corn-like titanium nitride nanostructures, Adv. Sci. 3 (2016), https://doi.org/10.1002/advs.201500299.

[16] J. Riaz, J. Cao, Y. Zhang, A. Bibi, X. Zhou, Facile synthesis and electrochemical analysis of TiN-based ZnO nanoparticles as promising cathode materials for asymmetric supercapacitors, Nanoscale Adv. 6 (2024) 5145–5157, https://doi.org/10.1039/D4NA00372A.

[17] W. Yao, P. Makowski, C. Giordano, F. Goettmann, Synthesis of early-transition-metal carbide and nitride nanoparticles through the urea route and their use as alkylation catalysts, Chem. Eur. J. 15 (2009) 11999–12004, https://doi.org/10.1002/chem.200901496.

[18] T. Wang, K. Li, S. An, C. Song, X. Guo, Facile and green synthesis of TiN/C as electrode materials for supercapacitors, Appl. Surf. Sci. 470 (2019) 241–249, https://doi.org/10.1016/j.apsusc.2018.11.088.

[19] L. Yu, B. Liu, Y. Wang, F. Yu, J. Ma, Recent progress on MXene-derived material and its' application in energy and environment, J. Power Sources 490 (2021) 229250, https://doi.org/10.1016/j.jpowsour.2020.229250.

[20] S. Ali, M. Sufyan Javed, K. Umer, J. Wang, Y. Fu, S. Kong, S. Khan, A. Ahmad, A. Parkash, M.D. Albaqami, Annu, J. Qi, D. He, MoS2@Ti3C2T heterostructure: a new negative electrode material for Li-ion hybrid supercapacitors, Chem. Eng. J. 498 (2024) 155330, https://doi.org/10.1016/j.cej.2024.155330.

[21] S. Park, S.H. Choi, J.M. Kim, S. Ji, S. Kang, S. Yim, S. Myung, Seong.K. Kim, S. S. Lee, K. An, Nanoarchitectonics of MXene derived TiO 2 /graphene with vertical alignment for achieving the enhanced supercapacitor performance, Small 20 (2024), https://doi.org/10.1002/smll.202305311.

[22] X. Xu, Y. Wang, C. Wang, B. Cui, C. Wang, Multifunctional C/TiO2 from MXene/polyaniline for electromagnetic protection and supercapacitor, Energy Mater. Adv. 5 (2024), https://doi.org/10.34133/energymatadv.0070.

[23] P. Urbankowski, B. Anasori, K. Hantanasirisakul, L. Yang, L. Zhang, B. Haines, S. J. May, S.J.L. Billinge, Y. Gogotsi, 2D molybdenum and vanadium nitrides synthesized by ammoniation of 2D transition metal carbides (MXenes), Nanoscale 9 (2017) 17722–17730, https://doi.org/10.1039/C7NR06721F.

[24] Y. Fan, K. Liu, A. Ali, X. Chen, P.K. Shen, 2D TiN@C sheets derived from MXene as highly efficient polysulfides traps and catalysts for lithium−sulfur batteries, Electrochim. Acta 384 (2021) 138187, https://doi.org/10.1016/j.electacta.2021.138187.

[25] C. Huber, S.S. Jahromy, F. Birkelbach, J. Weber, C. Jordan, M. Schreiner, M. Harasek, F. Winter, The multistep decomposition of boric acid, Energy Sci. Eng. 8 (2020) 1650–1666, https://doi.org/10.1002/ese3.622.

[26] A. Rotaru, Thermal and kinetic study of hexagonal boric acid versus triclinic boric acid in air flow, J. Therm. Anal. Calorim. 127 (2017) 755–763, https://doi.org/10.1007/s10973-016-5583-7.

[27] Y. Wang, C. Wang, Y. Wang, H. Liu, Z. Huang, Boric acid assisted reduction of graphene oxide: a promising material for sodium-ion batteries, ACS Appl. Mater. Interfaces 8 (2016) 18860–18866, https://doi.org/10.1021/acsami.6b04774.

[28] H. Zhang, X. Du, G. Li, Effect of encapsulation of boron nanoparticles using reduced graphene oxide on their oxidation characteristics, Propellants, Explos., Pyrotech. 46 (2021) 1240–1247, https://doi.org/10.1002/prep.202100004.

[29] K.J. Cai, Y. Zheng, P. Shen, S.Y. Chen, TiC x –Ti 2 C nanocrystals and epitaxial graphene-based lamellae by pulsed laser ablation of bulk TiC in vacuum, CrystEngComm 16 (2014) 5466–5474, https://doi.org/10.1039/C4CE00358F.

[30] O. Frank, M. Zukalova, B. Laskova, J. Kürti, J. Koltai, L. Kavan, Raman spectra of titanium dioxide (anatase, rutile) with identified oxygen isotopes (16, 17, 18), Phys. Chem. Chem. Phys. 14 (2012) 14567, https://doi.org/10.1039/c2cp42763j.

[31] G. Lota, P. Krawczyk, K. Lota, A. Sierczyńska, Ł. Kolanowski, M. Baraniak, T. Buchwald, The application of activated carbon modified by ozone treatment for energy storage, J. Solid State Electrochem. 20 (2016) 2857–2864, https://doi.org/10.1007/s10008-016-3293-5.

[32] M. Han, X. Yin, H. Wu, Z. Hou, C. Song, X. Li, L. Zhang, L. Cheng, Ti 3 C 2 MXenes with modified surface for high-performance electromagnetic absorption and shielding in the X-band, ACS Appl. Mater. Interfaces 8 (2016) 21011–21019, https://doi.org/10.1021/acsami.6b06455.

[33] O.B. Nazarenko, T.V. Melnikova, P.M. Visakh, Combined effect of zeolite and boric acid on thermal behavior of epoxy composites, J. Therm. Anal. Calorim. 128 (2017) 169–175, https://doi.org/10.1007/s10973-016-5901-0.

[34] J. Ulbricht, R. Jordan, R. Luxenhofer, On the biodegradability of polyethylene glycol, polypeptoids and poly(2-oxazoline)s, Biomaterials 35 (2014) 4848–4861, https://doi.org/10.1016/j.biomaterials.2014.02.029.

[35] P.R. Kidambi, B.C. Bayer, R. Blume, Z.-J. Wang, C. Baehtz, R.S. Weatherup, M.-G. Willinger, R. Schloegl, S. Hofmann, Observing graphene grow: catalyst–graphene interactions during scalable graphene growth on polycrystalline copper, Nano Lett. 13 (2013) 4769–4778, https://doi.org/10.1021/nl4023572.

[36] A. Carvalho, M.C.F. Costa, V.S. Marangoni, P.R. Ng, T.L.H. Nguyen, A.H. Castro Neto, The degree of oxidation of graphene oxide, Nanomaterials 11 (2021) 560, https://doi.org/10.3390/nano11030560.

[37] R.B. Rakhi, B. Ahmed, M.N. Hedhili, D.H. Anjum, H.N. Alshareef, Effect of postetch annealing gas composition on the structural and electrochemical properties of Ti 2 CT *x* MXene electrodes for supercapacitor applications, Chem. Mater. 27 (2015) 5314–5323, https://doi.org/10.1021/acs.chemmater.5b01623.

[38] J. Yesuraj, J. Kim, R. Yang, K. Kim, Deoxyribonucleic acid scaffolded and encapsulated one-dimensional gadolinium(III) hydroxide nanorods for supercapacitors and oxygen evaluation reaction properties, Adv. Compos. Hybrid Mater. 7 (2024) 69, https://doi.org/10.1007/s42114-024-00881-y.

[39] S. Roguai, A. Lakel, A. Djelloul, K. Lalmi, N. Kamoun-Turki, Enhancement of titanium nitride-specific capacitance using rapid thermal sulfurization, J. Mater. Eng. Perform. 34 (2025) 576–582, https://doi.org/10.1007/s11665-023-09067-x.

[40] A. Achour, R. Lucio-Porto, M. Chaker, A. Arman, A. Ahmadpourian, M.A. Soussou, M. Boujtita, L. Le Brizoual, M.A. Djouadi, T. Brousse, Titanium vanadium nitride electrode for micro-supercapacitors, Electrochem. Commun. 77 (2017) 40–43, https://doi.org/10.1016/j.elecom.2017.02.011.

[41] A. Achour, R.L. Porto, M.-A. Soussou, M. Islam, M. Boujtita, K.A. Aissa, L. Le Brizoual, A. Djouadi, T. Brousse, Titanium nitride films for micro-supercapacitors: effect of surface chemistry and film morphology on the capacitance, J. Power Sources 300 (2015) 525–532, https://doi.org/10.1016/j.jpowsour.2015.09.012.

[42] H. Qi, S. Yick, O. Francis, A. Murdock, T. van der Laan, K. (Ken) Ostrikov, Z. Bo, Z. Han, A. Bendavid, Nanohybrid TiN/vertical graphene for high-performance

supercapacitor applications, Energy Storage Mater. 26 (2020) 138–146, https://doi.org/10.1016/j.ensm.2019.12.040.
[43] B. Wei, H. Liang, D. Zhang, Z. Wu, Z. Qi, Z. Wang, CrN thin films prepared by reactive DC magnetron sputtering for symmetric supercapacitors, J. Mater. Chem. A Mater. 5 (2017) 2844–2851, https://doi.org/10.1039/C6TA09985H.
[44] H. Cao, X. Peng, M. Zhao, P. Liu, B. Xu, J. Guo, Oxygen functional groups improve the energy storage performances of graphene electrochemical supercapacitors, RSC Adv. 8 (2018) 2858–2865, https://doi.org/10.1039/C7RA12425B.
[45] H.-J. Lee, A. Abdellah, F.M. Ismail, C. Gumeci, N. Dale, J. Parrondo, D.C. Higgins, Understanding the impact of nitrogen doping and/or amine functionalization of reduced graphene oxide via hydrothermal routes for supercapacitor applications, Electrochim. Acta 397 (2021) 139241, https://doi.org/10.1016/j.electacta.2021.139241.
[46] L. Sun, L. Wang, C. Tian, T. Tan, Y. Xie, K. Shi, M. Li, H. Fu, Nitrogen-doped graphene with high nitrogen level via a one-step hydrothermal reaction of graphene oxide with urea for superior capacitive energy storage, RSC Adv. 2 (2012) 4498, https://doi.org/10.1039/c2ra01367c.
[47] Y. Peng, Z. Chen, R. Zhang, W. Zhou, P. Gao, J. Wu, H. Liu, J. Liu, A. Hu, X. Chen, Oxygen-containing functional groups regulating the carbon/electrolyte interfacial properties toward enhanced K+ storage, Nanomicro Lett. 13 (2021) 192, https://doi.org/10.1007/s40820-021-00722-3.
[48] X.F. Sánchez-Romate, A. Del Bosque, J. Artigas-Arnaudas, B.K. Muñoz, M. Sánchez, A. Ureña, A proof of concept of a structural supercapacitor made of graphene coated woven carbon fibers: EIS study and mechanical performance, Electrochim. Acta 370 (2021), https://doi.org/10.1016/j.electacta.2021.137746.
[49] N.A. Cañas, K. Hirose, B. Pascucci, N. Wagner, K.A. Friedrich, R. Hiesgen, Investigations of lithium–sulfur batteries using electrochemical impedance spectroscopy, Electrochim. Acta 97 (2013) 42–51, https://doi.org/10.1016/j.electacta.2013.02.101.
[50] J. Bisquert, G. Garcia-Belmonte, P. Bueno, E. Longo, L.O.S. Bulhões, Impedance of constant phase element (CPE)-blocked diffusion in film electrodes, J. Electroanal. Chem. 452 (1998) 229–234, https://doi.org/10.1016/S0022-0728(98)00115-6.
[51] X.F. Sánchez-Romate, A. Del Bosque, J. Artigas-Arnaudas, B.K. Muñoz, M. Sánchez, A. Ureña, A proof of concept of a structural supercapacitor made of graphene coated woven carbon fibers: EIS study and mechanical performance, Electrochim. Acta 370 (2021) 137746, https://doi.org/10.1016/j.electacta.2021.137746.
[52] E. Pranada, D. Johnson, R. Yoo, A. Djire, Subsurface oxygen reduction reaction activity on Ti 2 N MXene revealed by *in situ* Raman spectroelectrochemistry, Sustain. Energy Fuels 7 (2023) 956–964, https://doi.org/10.1039/D2SE01532C.
[53] Y. Sun, J. Gao, X. Du, X. Zhu, Rapid and precise fabrication of a three-dimensional, high-capacity, asymmetric micro-supercapacitor utilizing mortise-and-tenon joint construction, New J. Chem. 49 (2025) 14866–14873, https://doi.org/10.1039/D5NJ02143J.
[54] K.-H. Lee, S.-S. Lee, D.B. Ahn, J. Lee, D. Byun, S.-Y. Lee, Ultrahigh areal number density solid-state on-chip microsupercapacitors via electrohydrodynamic jet printing, Sci. Adv. 6 (2020), https://doi.org/10.1126/sciadv.aaz1692.
[55] P. Yadav, A. Basu, A. Suryawanshi, O. Game, S. Ogale, Highly stable laser-scribed flexible planar microsupercapacitor using mushroom derived carbon electrodes, Adv. Mater. Interfaces 3 (2016), https://doi.org/10.1002/admi.201600057.
[56] G. Wang, H. Wang, X. Lu, Y. Ling, M. Yu, T. Zhai, Y. Tong, Y. Li, Solid-state supercapacitor based on activated carbon cloths exhibits excellent rate capability, Adv. Mater. 26 (2014) 2676–2682, https://doi.org/10.1002/adma.201304756.
[57] Z. Peng, R. Ye, J.A. Mann, D. Zakhidov, Y. Li, P.R. Smalley, J. Lin, J.M. Tour, Flexible boron-doped laser-induced graphene microsupercapacitors, ACS Nano 9 (2015) 5868–5875, https://doi.org/10.1021/acsnano.5b00436.
[58] R. Wang, C. Xia, N. Wei, H.N. Alshareef, NiCo2O4@TiN Core-shell electrodes through conformal atomic layer deposition for all-solid-state supercapacitors, Electrochim. Acta 196 (2016) 611–621, https://doi.org/10.1016/j.electacta.2016.03.015.
[59] X. Lu, G. Wang, T. Zhai, M. Yu, S. Xie, Y. Ling, C. Liang, Y. Tong, Y. Li, Stabilized TiN nanowire arrays for high-performance and flexible supercapacitors, Nano Lett. 12 (2012) 5376–5381, https://doi.org/10.1021/nl302761z.
[60] P. Qin, X. Li, B. Gao, J. Fu, L. Xia, X. Zhang, K. Huo, W. Shen, P.K. Chu, Hierarchical TiN nanoparticles-assembled nanopillars for flexible supercapacitors with high volumetric capacitance, Nanoscale 10 (2018) 8728–8734, https://doi.org/10.1039/C8NR01485J.
[61] S. Wang, C. Sun, Y. Shao, Y. Wu, L. Zhang, X. Hao, Self-supporting GaN nanowires/graphite paper: novel high-performance flexible supercapacitor electrodes, Small 13 (2017), https://doi.org/10.1002/smll.201603330.